LAWRENCE
LIVERMORE
NATIONAL
LABORATORY

LLNL-TR-671138

Implementation of an anisotropic mechanical model for shale in Geodyn

A. Attia, O. Vorobiev, S. Walsh

May 21, 2015

Disclaimer

This work performed under the auspices of the U.S. Department of Energy by Lawrence Livermore National Laboratory under Contract DE-AC52-07NA27344.

Implementation of an anisotropic mechanical model for shale in Geodyn

Armand Attia, Oleg Vorobiev and Stuart Walsh
May 26, 2015
LLNL-TR-671138

Disclaimer

This work was performed under the auspices of the U.S. Department of Energy by Lawrence Livermore National Laboratory under Contract DE-AC52-07NA27344.

1 Introduction

Modeling of fracture of shales during drilling and hydraulic fracturing is a major research area for gas and oil industries [1, 2, 3, 4].

Due to their laminate structure, shales exhibit an anisotropic mechanical response which has been ignored for long time. Yet, recently there have been a few attempts to develop and use orthotropic models for shales [5, 4].

The purpose of this report is to present the implementation of a shale model in the Geodyn code, based on published rock material models and properties that can help a petroleum engineer in his design of various strategies for oil/gas recovery from shale rock formation. Drilling strategies may include using explosives for fracturing rock and injection of proppants for maintainting fractures open. During drilling, borehole stability is an important concern, requiring an understanding of natural shale layered structure, elastic moduli, strength, pore fluid pressure, mineral content, etc

To account for the layered shale structure, which can be on a very small scale, an anisotropic model is necessary to calculate rock response to applied loading. Where explosives are used to break up the rock, porosity and compaction need to be modeled, and the model needs to be sensitive to relatively high strain rate. Far away from the explosion site, the rock is subject to lower strain rates, so that strain-rate sensitivity is not an issue.

A petroleum engineer has a variety of tools at his disposal in developing his strategy. These tools include measuring rock properties (logging) at various depths, extracting rock samples for laboratory measurements (e.g. triaxial tests). To evaluate borehole stability, techniques may range, for example, from calculating borehole collapse pressure using analytical models [6] to FEM codes that incorporate constitutive models, such as [5]. Both types of techniques require validation with experimental data. The focus of this report will be mainly on constitutive models (used in FEM codes) using parameters that can be calibrated to rock tests, and a collection of available data for such tests. The Crook model [5] has been identified as a complete anisotropic model that can be used as a good starting point.

In this report, we review several approaches to modeling shale and then focus on the implementation of a particular model (the Crook anisotropic model).

2 Models applied to blast loading

The first papers will illustrate capabilities and limitations of isotropic models used to calculate rock behavior under explosive loading. Grady and Kipp in [7], Kipp and Grady in [8], Kipp, Grady, Chen in [9] show

good agreement between experimental and analytical results finding that fracture stress and energy increase with strain rate while fragment size decreases with strain rate, using only isotropic damage models. However, Taylor, Chen, Kuszmaul in [10] find that isotropic models with or without layering are only able to reproduce the peak values of measured stress waves but not the release history.

Zhang, Hao, Lu in [11] argue that an anisotropic damage model is needed but their results for fracture stress and fragment size are just as good as those obtained by Grady et al, in the previous papers, for the same data.

3 Models applied to triaxial tests

The next set of papers apply various anisotropic formulations to triaxial tests.

Nova [12] assumes linear transverse isotropic elasticity, with an anisotropic yield, associative plastic flow, and strain-hardening, in an extended cam-clay model, intended for soft rocks. While the model gives good agreement with experiment for longitudinal stiffness, triaxial test simulations do not agree well with experimental data. Specifically, the model gives poor agreement with experiment for stress-difference (S_1-S_3) vs. strain.

Niandou et al [13] were able to correct this deficiency in Nova's model by allowing for non-associative flow (with a plastic potential distinct from the yield) in order to match their Tournemire shale data [14].

Cazacu and Cristescu [15] developed a failure model, based on an anisotropic Mises-Schleicher failure criterion, which agrees very well with Tournemire data for the variation of failure stress with orientation and for various confining pressures, where the orientation angle is defined for the principal stress system with respect with the material symmetry structural system. They also present an anisotropic model [2] in which they use extensive fitting to formulate elastic parameters and a yield surface. The expression for the yield surface is initially unknown and is fully determined from experimental data.

Tien [16] studies the failure stress of artificially layered material. He introduces a failure criterion based on two modes of failure: sliding on a discontinuity across material layers and failure within a single layer without sliding. Tien identifies an anisotropy parameter n defined by:

$$n = \frac{E}{2G} - \nu \tag{1}$$

which is equal to 1 for isotropic material. E is Young's modulus at 90 degrees with respect to the intrinsic material frame and G and ν

are the shear modulus and Poisson's ratio, in the same frame. For Martinsburg shale, he finds that this parameter varies only from 3.5 to 4.6 over confining pressures ranging widely from 3.5 MPa to 100 MPa. He obtains good agreement for the Tournemire data.

Pietruszczak et al[17] develops an intricate anisotropic model with microstructure without damage, which shows moderate agreement for stress difference vs. volumetric strain for the Tournemire data.

Gao et al [18] present an anisotropic failure criterion, in which they introduce a fabric tensor to achieve some success in the calculation of the friction angle, giving clearly better results than an isotropic model. Their model does quite well on Tournemire shale, predicting correctly the variation in shear strength for various loading orientations. They provide a calibration procedure for the parameters introduced in the failure criterion. Note that they do not present the entire model, but only the failure criterion.

Chen et al [19] also introduce a fabric tensor in their anisotropic damage model, in which they couple plastic deformation with damage induced by growth of microcracks. They also draw on the work of Pietruszczak in their formulation. They obtain good agreement with their model on the Tournemire shale data. This is an advanced model, allowing for the yield to depend on stress, scalar measure of plastic strain, density of microcracks, and a scalar anisotropy parameter, which represents the projection of a microstructure tensor on the current loading direction.

Chen et al [20] discuss the coupling between inherent and induced anisotropy in sedimentary rocks, using a fabric tensor to characterize anisotropic behavior.They obtain good agreement on shear stress vs. strain for the Tournemire shale data. This is also a very advanced model, which allows for friction coefficient and material cohesion for a family of weakness planes.

Hu et al [21] add the effect of water content to the anisotropic modeling. They provide calibration of model parameters and show good agreement with Tournemire argilite data for triaxial tests, except for volumetric strain vs. axial strain. Capillary pressure is introduced to describe the effect of the water content, using the effective stress concept. The model represents random microcracks by several families of parallel penny-shaped microcracks. The overall plastic strain is defined as an average weighted by microcrack density.

Lisjak et al [22] addresses brittle failure of anisotropic Opalinus Clay with a transversely isotropic constitutive model. Model parameters are calibrated with uniaxial compresive strength tests and Brazil disc tests.Their model shows good agreement with experimental data for maximum principal failure stress vs. confining pressure. With their FEM-DEM method, they are able to calculate crack patterns for various orientations.

4 Sample properties from literature

Dewhurst et al [23] provide several interesting correlations of shale properties from a variety of geographical locations. Figure 1 shows correlation between unconfined compressive strength and porosity. Figure 2 shows a tight correlation between P-wave velocity and porosity.

Sone et al [24] provide properties of Barnett and Haynesville shale. Figure 3 shows sample mineral composition, frictional coefficients, unconfined compressive strengths. Figure 4 shows Young's modulus and Poisson's ratio.

Li et al [25] give shale strength data for Haynesville site. Figure 5 shows the effect of confining pressure on shale strength.

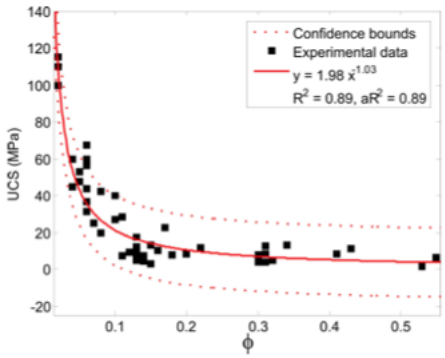

Figure 1: UCS vs. Porosity [23]

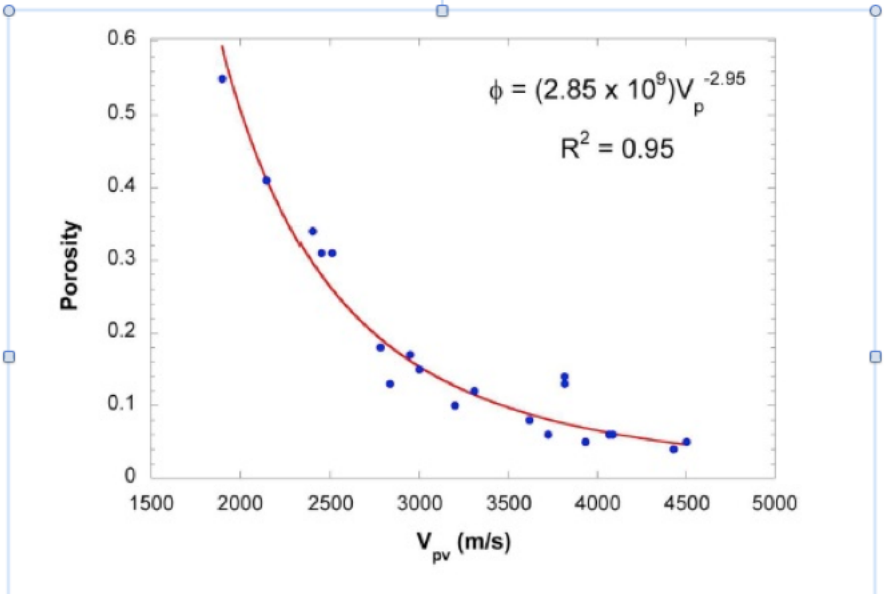

Figure 2: P-wave velocity vs. Porosity [23]

Sample Group	Qtz/Felds [%]	Carbonate [%]	Clay [%]	Others [%]	Pc Triax [MPa]	Creep Stress 1st/2nd step [MPa]	Frictional Coefficient	UCS [MPa]
Barnett Dark	60	10	25	5	30	-	0.923	160
					30	46.5 / 92.0	0.805	
					30	46.5 / 92.1	0.706	
					20	47.3 / 95.2	0.899	
					30	-	0.896	
					40	49.2 / 94.9	0.791	
Barnett Light	35	55	5	5	30	-	0.928	220
					20	44.7 / 89.7	1.10	
					40	48.6 / 94.0	-	
Haynesville Dark	45	13	39	3	60	-	0.534	120
					60	29.4 / 58.4	0.539	
					30	32.1 / 61.0	0.599	
					20	31.0 / 60.0	0.686	
					30	35.5 / 64.6	0.643	
Haynesville Light	28	48	22	2	60	-	0.675	160
					30	37.1 / 77.1	0.745	
					20	34.4 / 74.6	0.822	

Figure 3: Sample mineral composition and mechanical properties [24]

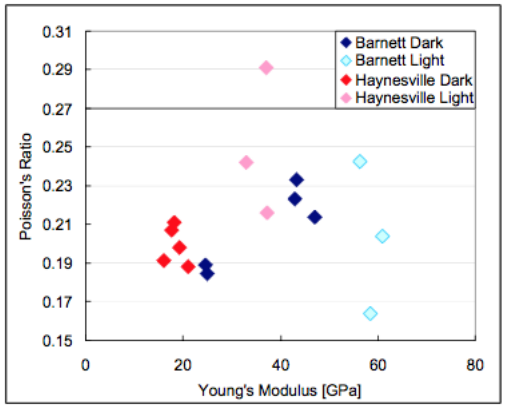

Figure 4: Sample Young's modulus and Poisson ratio [24]

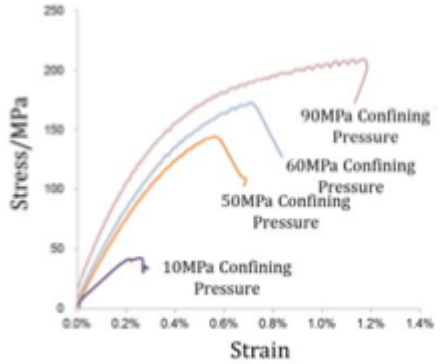

Figure 5: Effect of confining pressure on shale strength [25]

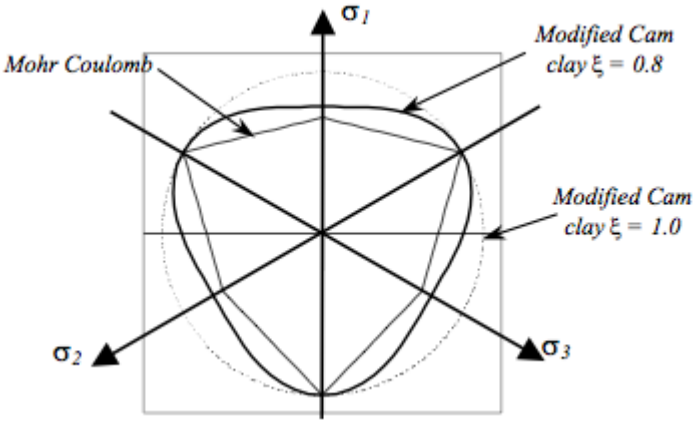

Figure 6: Adjusting yield surface for anisotropic shale [5]

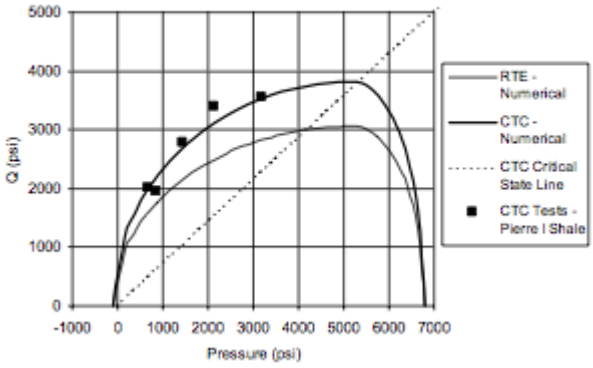

Figure 7: Equivalent stress vs. pressure for Modified Cam Clay model [5]

5 Crook Anisotropic Model

Crook et al [5] draw from the work of Cazacu and Pietruszczak and present an anisotropic model based on extending the isotropic modified Cam Clay critical state model to allow orthotropic elasticity, an orthotropic pressure dependent yield surface, and hardening/softening governed by the evolution of volumetric plastic strain. Triaxial compression tests are used to validate the model. The model is applied for prediction of equivalent stress q vs. axial/radial strain. The model is successful in predicting peak values but has difficulty with the subsequent release. Nevertheless, this model appears to be a good candidate for a first implementation, given what is attempted in the formulation, which avoids the complexity of Pietruszczak's approach. The same model has also been used by Soreide et al [3]

to evaluate borehole stability, using Abaqus to implement the model. Crook et al realize that for induced anisotropy due to oriented growth of microcracks, a fabric tensor with an evolution law are needed. This is not included in their model. See the work of Chen [20] above. The effect of pore fluid pressure will require using a formulation sensitive to anisotropy, as described by Carroll [26] and by Chen and Nur [27] . See also the work of Hu et al [21], above.

Crook et al have adapted the Modified Cam Clay model for shale. Figure 6 shows the modified Cam Clay yield surface, and Figure 7 shows the corresponding representation for equivalent stress vs. pressure, thus resulting in a good fit with experimental data. The material parameters are calibrated by back-analysis of uniaxial and triaxial tests. The elastic parameters are determined from conventional triaxial tests as follows. Young's modulus normal to bedding plane and out-of-plane Poisson's ratio are determined from triaxial tests with horizontal bedding planes. In-plane Young's modulus and Poisson's ratio are determined from triaxial tests with vertical bedding planes. Out-of-plane shear modulus is estimated from St. Venant's formula [14].

The modified Cam Clay yield surface requires four parameters: pre-consolidation pressure p_c, tensile intercept p_t, slope of critical state line M, and consolidation cap shape parameter β. The slope M is determined from the ratio of equivalent stress to pressure at constant plastic volume from triaxial compression and extension data. The pressures p_c and p_t are the positive and negative intercepts of the projection of the yield surface in pressure-equivalent stress space. From triaxial data for various void volumes (i.e. plastic volumetric strain), a linear fit is determined for the variation of p_c and p_t with plastic volume. The parameter β is chosen based on previous work with sandstone.

The transverse isotropic yield surface defines the failure criterion and requires three parameters which are determined from unconfined compressive strengths from triaxial tests with differing bedding plane orientations. The model is calibrated to fit the experiment at orientations of 0, 45, and 90 degrees.

Finally, a characteristic length scale is required in order to reproduce the correct dependence of strength on specimen size. This parameter is used to scale the inelastic strain and is typically the grain size of the shale. Crook et al set this parameter to 0.05 " in their work on Pierre shale.

The next sections of this report describe the Crook model as implemented in the Geodyn code. After describing the constitutive coefficients for transversely isotropic material, we describe how to transform the constitutive matrix from the intrinsic "bedding" frame to an arbitrary laboratory Eulerian frame and how to calculate wave

speeds. Next, we show that, using these transformations, we recover the correct Young's modulus for loading either normal or parallel to the isotropic bedding plane. The next two sections cover the elasto-plastic model for isotropic and anisotropic yield criteria. The latter is a simplified version of Crook's anisotropic yield. A sample 1-zone calculation is shown for tri-axial compression using the isotropic yield, illustrating the role of volumetric plastic strain in the hardening or softening of the yield strength. A porosity model is introduced based on Wood's model [28, 29], setting the stage for adding pore fluid pressure later. A Newton-Raphson scheme is added, using radial return to get a first estimate for the stress iterate, giving excellent satisfaction of the yield criterion. Finally, we make some comments on the implementation and describe both input parameters and output state variables.

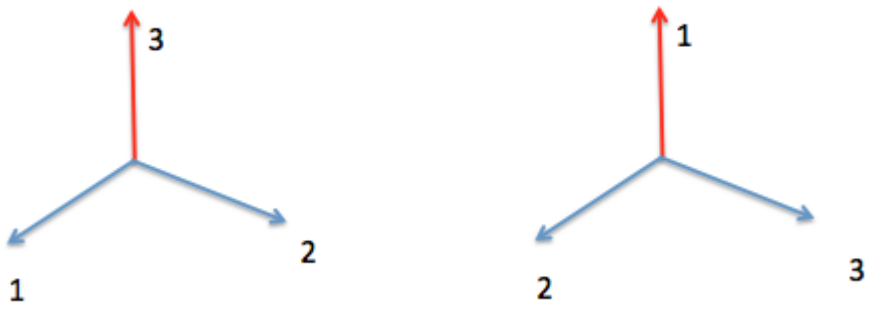

Figure 8: Transverse Isotropy Frames: Bower (left) and Crook (right)

6 Elasticity relations

6.1 Trial elastic stress

For a given strain increment $\Delta\epsilon$ and the transversely isotropic elasticity matrix C, write the trial stress (including stress at previous time step n and Jaumann stress flux) as (assume that stress is positive in compression as usual in rock mechanics):

$$\tilde{\boldsymbol{\sigma}} = \boldsymbol{\sigma_n} + \mathbf{C}\Delta\boldsymbol{\epsilon} + (\boldsymbol{W_{n+1}}\boldsymbol{\sigma_n} - \boldsymbol{\sigma_n}\boldsymbol{W_{n+1}})\boldsymbol{\Delta} t \tag{2}$$

6.2 Elasticity matrix

The elasticity stiffness matrix C is given by Bower in [30] (p. 84) with respect to a Bower frame, as shown in Figure 8. In this Bower frame (elsewhere referred to as the "bedding" frame), the "1-2" plane is the isotropic bedding plane, while the "3" axis is normal to the bedding plane. Crook uses "2-3" for the isotropic bedding plane and the "1" axis normal to the bedding plane. Write with respect to the Bower frame:

$$\hat{\sigma}_\alpha = \hat{C}_{\alpha\beta}\hat{\epsilon}_\beta \tag{3}$$

in which α and β range from 1 to 6. The stress components are represented as vectors, following Voigt ordering: [11 22 33 23 13 12]. The strain components follow the same ordering, except that:

$$\hat{\epsilon}_4 = 2\hat{\epsilon}_{23} \tag{4}$$

$$\hat{\epsilon}_5 = 2\hat{\epsilon}_{31} \tag{5}$$

$$\hat{\epsilon}_6 = 2\hat{\epsilon}_{12} \tag{6}$$

This is necessary for the constitutive matrix to be symmetric [31].

With the Bower frame and the Voigt ordering, the elasticity matrix for transverse isotropy has the structure given by Bower [30] as:

$$\boldsymbol{C} = \begin{pmatrix} \hat{C}_P & O \\ O & \hat{C}_G \end{pmatrix} \tag{7}$$

in which the subscript "P" refers to the part of the matrix relating [11 22 33] components, the subscript "G" refers to the part of the matrix relating [23 13 12] components. Within the Bower frame, elastic coefficients associated with the bedding plane will be labeled with the subscript "2" (interchangeable with subscript "1"). The subscript "3" will be associated with the transverse axis normal to the bedding (isotropic) plane. Then, $\hat{C}_P$ is given by:

$$\boldsymbol{C_P} = \begin{pmatrix} \hat{C}_{11} & \hat{C}_{12} & \hat{C}_{13} \\ \hat{C}_{12} & \hat{C}_{11} & \hat{C}_{13} \\ \hat{C}_{13} & \hat{C}_{13} & \hat{C}_{33} \end{pmatrix} \tag{8}$$

where:

$$\hat{C}_{11} = AE_2(1 - \nu_{23}\nu_{32}) \tag{9}$$
$$\hat{C}_{12} = AE_2(\nu_{12} + \nu_{23}\nu_{32})) \tag{10}$$
$$\hat{C}_{13} = AE_2\nu_{32}(1 + \nu_{12}) \tag{11}$$
$$\hat{C}_{33} = AE_3(1 - \nu_{12}^2) \tag{12}$$
$$A^{-1} = (1 - \nu_{12} - 2\nu_{23}\nu_{32})(1 + \nu_{12}) \tag{13}$$

In order for the stiffness matrix to be symmetric, the following must hold:

$$\frac{\nu_{32}}{E_3} = \frac{\nu_{23}}{E_2} \tag{14}$$

$\hat{C}_G$ is given by:

$$\boldsymbol{C_G} = \begin{pmatrix} \hat{C}_{44} & O & O \\ O & \hat{C}_{44} & O \\ O & O & \hat{C}_{66} \end{pmatrix} \tag{15}$$

where:

$$\hat{C}_{44} = G_3 \tag{16}$$
$$\hat{C}_{66} = G_2 = \frac{E_2}{2(1 + \nu_{12})} \tag{17}$$

G_3 is given by St. Venant's formula [32] as:

$$\frac{1}{G_3} = \frac{1}{E_3} + \frac{1}{E_2} + 2\frac{\nu_{32}}{E_3} \tag{18}$$

The elasticity matrix coefficients will be written with respect to the bedding frame and the Voigt order. The correspondence between the bedding frame coefficients and the Crook frame (superscript "C") is shown below:

$$E_2 = E_2^C \tag{19}$$
$$E_3 = E_1^C \tag{20}$$
$$\nu_{12} = \nu_{23}^C \tag{21}$$
$$\nu_{32} = \nu_{12}^C \tag{22}$$
$$\nu_{23} = \nu_{21}^C \tag{23}$$
$$G_2 = G_2^C \tag{24}$$
$$G_3 = G_1^C \tag{25}$$

6.3 Coordinate transformation for strike orientation and dip inclination

Figure 9 shows conventional definition of strike orientation and dip inclination. Figure 10 shows basis vectors e_S along strike axis at strike angle θ_S relative to reference North direction (measured clockwise from North) and associated vector e_A perpendicular to e_S. Figure 11 shows basis vector e_B normal to the bedding plane, rotated by the dip angle θ_D (measured counter-clockwise from the horizontal axis e_A) about the strike axis e_S. Now proceed to derive the coordinate transformation relating e_S and e_B to the Bower frame in Figure 8. For this purpose, relabel the strike axis e_S as $\hat{e}_1$ and the bedding normal e_B as $\hat{e}_3$. Within the isotropic bedding plane, the basis will be completed with the vector $\hat{e}_2 = \hat{e}_3 \times \hat{e}_1$. From the geometry in Figure 10 and Figure 11, we have:

$$\hat{\boldsymbol{e}}_i = \boldsymbol{Q}_{ij}\boldsymbol{e}_j \tag{26}$$

$$\boldsymbol{Q} = \begin{pmatrix} sin(\theta_S) & cos(\theta_S) & 0 \\ -cos(\theta_D)cos(\theta_S) & cos(\theta_D)sin(\theta_S) & sin(\theta_D) \\ sin(\theta_D)cos(\theta_S) & -sin(\theta_D)sin(\theta_S) & cos(\theta_D) \end{pmatrix} \tag{27}$$

Note: Since the strike angle is referred to the North axis ($\hat{e}_2$), to align the Bower frame with the bedding frame, set the dip angle $\theta_D = 0$ and the strike angle $\theta_S = 90^o$.

6.3.1 Longitudinal wave speed

Thomsen [33] shows that the maximum longitudinal wave speed corresponds to a wave normal lying in the bedding plane, thus at 90 degrees with the normal axis to the bedding plane. For an equivalent but clearer formulation see:

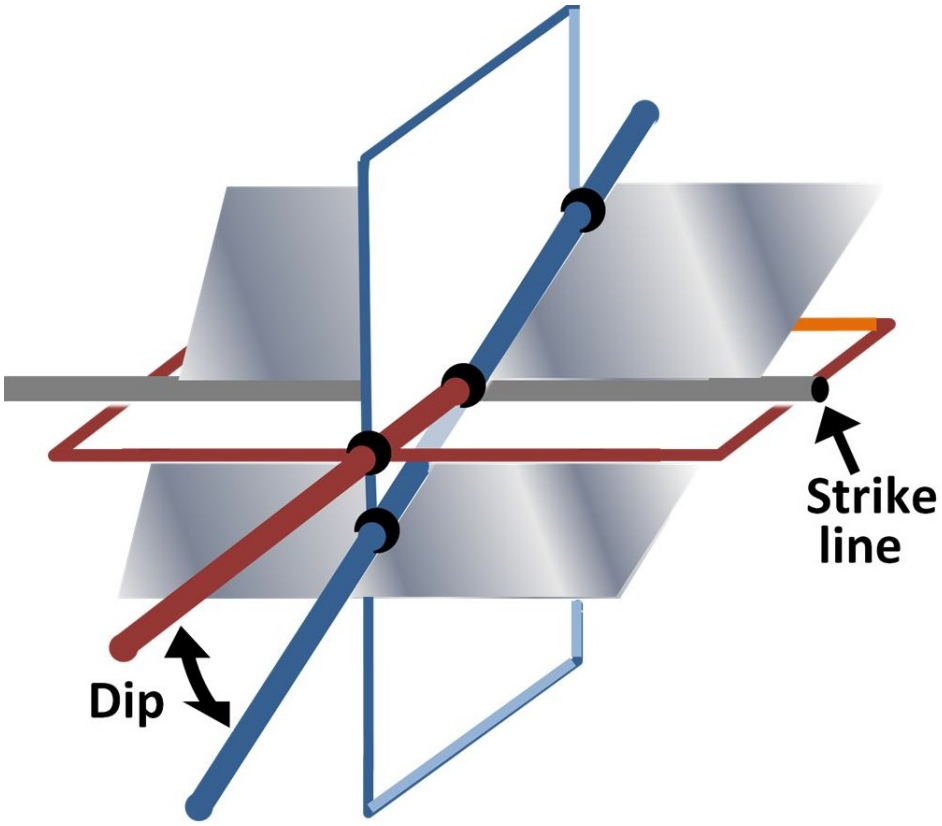

Figure 9: Strike and Dip conventions

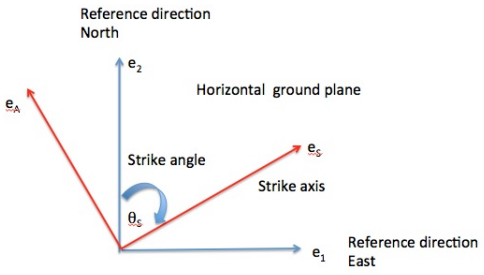

Figure 10: Basis vectors in horizontal plane

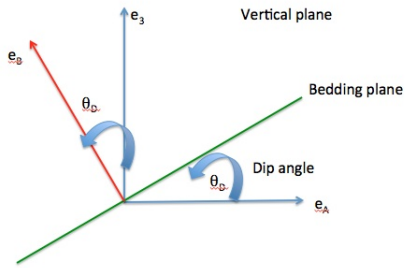

Figure 11: Basis vectors in vertical dip plane

`http://en.wikipedia.org/wiki/Transverse_isotropy`
`#Short_and_medium_wavelength_approximation`

where the longitudinal wave speed is given by:

$$\rho v_P^2(\theta) = \frac{1}{2}\Big(\hat{C}_{11}sin^2(\theta) + \hat{C}_{33}cos^2(\theta) + \hat{C}_{44} + \sqrt{M(\theta)}\Big) \quad (28)$$

$$M(\theta) = \big[(\hat{C}_{11} - \hat{C}_{44})sin^2(\theta) - (\hat{C}_{33} - \hat{C}_{44})cos^2(\theta)\big]^2 + (\hat{C}_{13} + \hat{C}_{44})^2 sin^2(2\theta) \quad (29)$$

where θ is the angle between the wave normal direction and the axis $\hat{e}_3$ perpendicular to the bedding plane. Thomsen [33] introduces two parameters to characterize the degree of anisotropy:

$$\epsilon = \frac{\hat{C}_{11} - \hat{C}_{33}}{2\hat{C}_{33}} \quad (30)$$

$$\delta = \frac{(\hat{C}_{13} + \hat{C}_{44})^2 - (\hat{C}_{33} - \hat{C}_{44})^2}{2\hat{C}_{33}(\hat{C}_{33} - \hat{C}_{44})} \quad (31)$$

For sufficiently small values of these parameters, the longitudinal wave speed becomes:

$$v_P(\theta) = \alpha_0\Big(1 + \delta sin^2(\theta)cos^2(\theta) + \epsilon sin^4(\theta)\Big) \quad (32)$$

$$\alpha_0 = \sqrt{\frac{\hat{C}_{33}}{\rho}} \quad (33)$$

For which the first and second derivatives are, respectively:

$$\frac{\partial v_P(\theta)}{\partial \theta} = \alpha_0\Big(sin(2\theta)(\delta cos(2\theta) + 2\epsilon sin^2(\theta))\Big) \quad (34)$$

$$\frac{\partial^2 v_P(\theta)}{\partial \theta^2} = \alpha_0\Big(2cos(2\theta)(\delta cos(2\theta) + 2\epsilon sin^2(\theta)) + sin(2\theta)(-2\delta sin(2\theta) + 2\epsilon sin(2\theta))\Big) \quad (35)$$

An extremum occurs at 90 degrees. For a maximum, the second derivative must be negative there, so that:

$$\delta < 2\epsilon \tag{36}$$

Using the expressions for the transversely isotropic constitutive coefficients, we can derive an expression to determine whether the second derivative will be negative. From the values for moduli and Poisson ratios used by Crook, we find that the second derivative is negative.

6.3.2 Effective shear modulus

Geodyn advances the solution of the conservation laws by performing sweeps along each Eulerian direction (x, y, z). The Riemann solver within Geodyn requires an effective shear modulus associated with the tangential sound speed, interpreted here as the speed of the transverse wave lying within the bedding plane. This speed is given by Thomsen [33] as v_{SH} by:

$$\rho v_{SH}^2(\theta) = \hat{C}_{66} sin^2(\theta) + \hat{C}_{44} cos^2(\theta) \tag{37}$$

and the angle θ is the angle between the wave front normal and the normal to the bedding plane. The wave front normal is interpreted here as each Eulerian direction $(\boldsymbol{e}_1, \boldsymbol{e}_2, \boldsymbol{e}_3)$ along which Geodyn sweeps to advance the solution of the conservation equations. The angle θ has therefore the three values $(\theta_1, \theta_2, \theta_3)$ given by the direction cosines, for $i = 1, 2, 3$:

$$cos(\theta_i) = \boldsymbol{e}_i \cdot \hat{\boldsymbol{e}}_3 \tag{38}$$

From Eq. 26:

$$\boldsymbol{e}_i = Q_{ij}^T \hat{\boldsymbol{e}}_j \tag{39}$$

so that:

$$cos(\theta_i) = \boldsymbol{e}_i \cdot \hat{\boldsymbol{e}}_3 = Q_{i3}^T \tag{40}$$

The effective shear modulus associated with each sweep is therefore given by, for $i = 1, 2, 3$:

$$G(\theta_i) = G_2 sin^2(\theta_i) + G_3 cos^2(\theta_i) \tag{41}$$

6.3.3 Transformation of constitutive coefficients

In this section, we derive the transformation from the bedding frame $\hat{e}_i$ to the laboratory (Eulerian) frame $\boldsymbol{e}_j$, with a strike angle of 90, for rotation θ_D about the $\boldsymbol{e}_3$ axis.

$$\hat{\boldsymbol{e}}_1 = cos(\theta_D)\boldsymbol{e}_1 + sin(\theta_D)\boldsymbol{e}_2 \tag{42}$$

$$\hat{\boldsymbol{e}}_2 = -sin(\theta_D)\boldsymbol{e}_1 + cos(\theta_D)\boldsymbol{e}_2 \tag{43}$$

$$\hat{\boldsymbol{e}}_3 = \boldsymbol{e}_3 \tag{44}$$

from which the required inverse transformation $\boldsymbol{R}$ is given by:

$$\boldsymbol{R} = \begin{pmatrix} 1 & 0 & 0 \\ 0 & cos(\theta_D) & -sin(\theta_D) \\ 0 & sin(\theta_D) & cos(\theta_D) \end{pmatrix} \tag{45}$$

The elastic stress-strain relation is given by:

$$\boldsymbol{\sigma} = \boldsymbol{C} : \boldsymbol{\epsilon} \tag{46}$$

However, the stress and strain are given with respect to the Eulerian frame, while the constitutive matrix is given with respect to the bedding frame. Therefore:

$$\sigma_{ij}\boldsymbol{e}_i\boldsymbol{e}_j = \hat{C}_{pqrs}\hat{\boldsymbol{e}}_p\hat{\boldsymbol{e}}_q\hat{\boldsymbol{e}}_r\hat{\boldsymbol{e}}_s : \epsilon_{kl}\boldsymbol{e}_k\boldsymbol{e}_l \tag{47}$$

$$\sigma_{ij} = R_{ip}R_{jq}\hat{C}_{pqrs}R_{kr}R_{ls}\epsilon_{kl} \tag{48}$$

$$R_{ip} = \boldsymbol{e}_i \cdot \hat{\boldsymbol{e}}_p \tag{49}$$

$$\sigma_{ij} = C_{ijkl}\epsilon_{kl} \tag{50}$$

$$C_{ijkl} = R_{ip}R_{jq}\hat{C}_{pqrs}R_{kr}R_{ls} \tag{51}$$

Mapping indices to Voigt space:

$$C_{\alpha\beta} = K_{\alpha\gamma}\hat{C}_{\gamma\delta}K^T_{\gamma\beta} \tag{52}$$

where $\boldsymbol{K}$ is given by [31]:

$$\boldsymbol{K} = \begin{pmatrix} \boldsymbol{K}_1 & 2\boldsymbol{K}_2 \\ \boldsymbol{K}_3 & \boldsymbol{K}_4 \end{pmatrix} \tag{53}$$

$$\boldsymbol{K}_1 = \begin{pmatrix} R_{11}^2 & R_{12}^2 & R_{13}^2 \\ R_{21}^2 & R_{22}^2 & R_{23}^2 \\ R_{31}^2 & R_{32}^2 & R_{33}^2 \end{pmatrix} \tag{54}$$

$$\boldsymbol{K}_2 = \begin{pmatrix} R_{12}R_{13} & R_{13}R_{11} & R_{11}R_{12} \\ R_{22}R_{23} & R_{23}R_{21} & R_{21}R_{22} \\ R_{32}R_{33} & R_{33}R_{31} & R_{31}R_{32} \end{pmatrix} \tag{55}$$

$$\boldsymbol{K}_3 = \begin{pmatrix} R_{21}R_{31} & R_{22}R_{32} & R_{23}R_{33} \\ R_{31}R_{11} & R_{32}R_{12} & R_{33}R_{13} \\ R_{11}R_{21} & R_{12}R_{22} & R_{13}R_{23} \end{pmatrix} \tag{56}$$

$$\boldsymbol{K}_4 = \begin{pmatrix} R_{22}R_{33} + R_{23}R_{32} & R_{23}R_{31} + R_{21}R_{33} & R_{21}R_{32} + R_{22}R_{31} \\ R_{32}R_{13} + R_{33}R_{12} & R_{33}R_{11} + R_{31}R_{13} & R_{31}R_{12} + R_{32}R_{11} \\ R_{12}R_{23} + R_{13}R_{22} & R_{13}R_{21} + R_{11}R_{23} & R_{11}R_{22} + R_{12}R_{21} \end{pmatrix} \tag{57}$$

The above transformations are used only when prescribing boundary stress conditions in a global frame. Otherwise, stresses and strains are transformed between the Eulerian (laboratory) frame and the bedding frame.

6.3.4 Verify vertical modulus perpendicular to bedding plane

Consider the transversely isotropic material oriented such that the normal to the bedding frame is aligned with the vertical direction. In this section, we show that for uniaxial (unconfined) axial vertical compression, with no lateral tractions, for this material orientation, the vertical Young's modulus is exactly E_3, as defined in the bedding frame. We have the elasticity equations:

$$\hat{\sigma}_\alpha = \hat{C}_{\alpha\beta}\hat{\epsilon}_\beta \tag{58}$$

subject to the conditions:

$$\hat{\sigma}_3 > 0 \tag{59}$$

and, for $\alpha \neq 3$:

$$\hat{\sigma}_\alpha = 0 \tag{60}$$

We now calculate the strains to satisfy these conditions and determine the modulus given by:

$$E = \frac{\hat{\sigma}_3}{\hat{\epsilon}_3} \tag{61}$$

to show that $E = E_3$. Applying the conditions $\hat{\sigma}_\alpha = 0$ for $\alpha = 1, 2$ in the elasticity equations gives the strains:

$$\hat{\epsilon}_1 = \hat{\epsilon}_2 = -\nu_{32}\hat{\epsilon}_3 \tag{62}$$

Substituting these strains in the elasticity equation for $\hat{\sigma}_3$

$$\hat{\sigma}_3 = \hat{C}_{3\beta}\hat{\epsilon}_\beta \tag{63}$$

gives the desired result.

$$\frac{\hat{\sigma}_3}{\hat{\epsilon}_3} = E_3 \tag{64}$$

6.3.5 Verify vertical modulus parallel to bedding plane

Now rotate the transversely isotropic material so that the bedding plane is aligned with the vertical direction, along which an axial load is applied, again with no lateral tractions. The dip angle is 90 degrees, for a rotation about the $\boldsymbol{e}_1$ axis of the material with respect to the fixed laboratory frame. Consequently, the transformation of basis vectors from $\hat{\boldsymbol{e}}_\alpha$ to $\boldsymbol{e}_\beta$ gives the relation:

$$\boldsymbol{e}_\alpha = \boldsymbol{R}_{\alpha\beta}\hat{\boldsymbol{e}}_\beta \tag{65}$$

where, with a strike angle of 90 degrees, we have:

$$\boldsymbol{R} = \begin{pmatrix} 1 & 0 & 0 \\ 0 & cos(\theta_D) & -sin(\theta_D) \\ 0 & sin(\theta_D) & cos(\theta_D) \end{pmatrix} \tag{66}$$

The uniaxial stress conditions are phrased with respect to the global laboratory frame. The elasticity equations in the global frame are:

$$\sigma_\alpha = C_{\alpha\beta}\epsilon_\beta \tag{67}$$

subject to the conditions:

$$\sigma_3 > 0 \tag{68}$$

and, for $\alpha \neq 3$:

$$\sigma_\alpha = 0 \tag{69}$$

Since the constitutive coefficients are defined in the basis $\hat{e}_\alpha$, they need to be transformed to the basis e_β via:

$$\boldsymbol{C} = \boldsymbol{K}\hat{\boldsymbol{C}}\boldsymbol{K}^T \tag{70}$$

where $\boldsymbol{K}$ is given by Ting in terms of the rotation matrix $\boldsymbol{R}$ renamed there as $\boldsymbol{\Omega}$. See Section 6.3.3 for more details. For this rotation of 90 degrees, the constitutive coefficients are transformed as follows:

$$C_{11} = \hat{C}_{11} \tag{71}$$
$$C_{12} = \hat{C}_{13} \tag{72}$$
$$C_{13} = \hat{C}_{12} \tag{73}$$
$$C_{22} = \hat{C}_{33} \tag{74}$$
$$C_{33} = \hat{C}_{11} \tag{75}$$

We now calculate the strains to satisfy these conditions and determine the modulus given by:

$$E = \frac{\sigma_3}{\epsilon_3} \tag{76}$$

to show that $E = E_2$. Applying the conditions $\sigma_\alpha = 0$ for $\alpha = 1, 2$ in the elasticity equations gives the strains:

$$\epsilon_1 = M_{13}\epsilon_3 \tag{77}$$
$$\epsilon_2 = M_{23}\epsilon_3 \tag{78}$$
$$M_{13} = (-1)(\frac{\hat{C}_{13}M_{23} + \hat{C}_{12}}{\hat{C}_{11}}) \tag{79}$$
$$M_{23} = \frac{\hat{C}_{13}(\hat{C}_{12} - \hat{C}_{11})}{\hat{C}_{11}\hat{C}_{33} - \hat{C}_{13}^2} \tag{80}$$

Substituting these strains in the elasticity equation for σ_3:

$$\sigma_3 = \hat{C}_{12}\epsilon_1 + \hat{C}_{13}\epsilon_2 + \hat{C}_{11}\epsilon_3 \tag{81}$$

or,

$$\sigma_3 = (\hat{C}_{12}M_{13} + \hat{C}_{13}M_{23} + \hat{C}_{11})\epsilon_3 \tag{82}$$

so that:

$$E = \frac{\sigma_3}{\epsilon_3} = \hat{C}_{12}M_{13} + \hat{C}_{13}M_{23} + \hat{C}_{11} \tag{83}$$

gives the desired result

$$\frac{\sigma_3}{\epsilon_3} = E_2 \tag{84}$$

For a particular calculation with the Geodyn driver, we must specify strain rates which satisfy the constraints of zero lateral stresses. For simplicity, we take $\nu_{12} = 0$. This choice results in $M_{23} = -\nu_{23}$ and $M_{13} = 0$. With $E_2 = 1.0$ GPa, $E_3 = 0.5$ GPa, $\nu_{23} = 0.25$, and $\dot{\epsilon}_3 = -1.0$ results in $\nu_{32} = 0.125$, $\dot{\epsilon}_1 = 0$, and $\dot{\epsilon}_2 = 0.25$, with strain rates per μsec.

6.3.6 Determining Poisson ratios

It is possible to determine Poisson ratios with respect to the bedding frame. From the UCS test at zero degrees:

$$E_3 = \frac{\sigma_3}{\epsilon_3} \tag{85}$$

$$\nu_{32} = -\frac{\epsilon_1}{\epsilon_3} \tag{86}$$

From the UCS test at 90 degrees,

$$E_2 = \frac{\sigma_3}{\epsilon_3} \tag{87}$$

$$\tag{88}$$

and ν_{12} measure the ratio of lateral extensions due to axial compression:

$$\nu_{12} = \nu_{32}\frac{E_2}{E_3}\frac{\epsilon_1}{\epsilon_2} \tag{89}$$

6.3.7 Issues with solution using stress decomposition

If we attempt to solve the above problem by first decomposing the stress into a pressure and a deviatoric stress, we will show here that we would require two different EOS forms, with different bulk moduli.

Typically, this decomposition is couched so that deviatoric stress is incremented. Therefore, we write:

$$\dot{\sigma}_{ij} = \dot{p}\delta_{ij} + \dot{S}_{ij} \tag{90}$$

where the deviatoric stress rate is the response to deviatoric strain rate:

$$\dot{S}_{ij} = C_{ijkl}(\dot{\epsilon}_{kl} - \frac{1}{3}\dot{\epsilon}_{mm}\delta_{kl}) \tag{91}$$

Conservation of mass requires (for strain positive in compression):

$$\dot{\rho} = \rho\dot{\epsilon}_{mm} \tag{92}$$

so that:

$$\dot{S}_{ij} = C_{ijkl}(\dot{\epsilon}_{kl} - \frac{1}{3}\frac{\dot{\rho}}{\rho}\delta_{kl}) = C_{ijkl}\dot{\epsilon}_{kl} - \frac{1}{3}\frac{\dot{\rho}}{\rho}C_{ijmm} \tag{93}$$

The requirements for the lateral stresses to vanish become:

$$\dot{S}_{11} = -\dot{p} \tag{94}$$

$$\dot{S}_{22} = -\dot{p} \tag{95}$$

so that:

$$\dot{S}_{11} = C_{11kl}\dot{\epsilon}_{kl} - \frac{1}{3}\frac{\dot{\rho}}{\rho}C_{11mm} = -\dot{p} \tag{96}$$

$$\dot{S}_{22} = C_{22kl}\dot{\epsilon}_{kl} - \frac{1}{3}\frac{\dot{\rho}}{\rho}C_{22mm} = -\dot{p} \tag{97}$$

In Voigt notation, this becomes (after applying the rotation transformation):

$$\dot{S}_1 = \hat{C}_{11}\dot{\epsilon}_1 + \hat{C}_{13}\dot{\epsilon}_2 + \hat{C}_{12}\dot{\epsilon}_3 - \frac{1}{3}\frac{\dot{\rho}}{\rho}(\hat{C}_{11} + \hat{C}_{12} + \hat{C}_{13}) = -\dot{p} \tag{98}$$

$$\dot{S}_2 = \hat{C}_{13}\dot{\epsilon}_1 + \hat{C}_{33}\dot{\epsilon}_2 + \hat{C}_{12}\dot{\epsilon}_3 - \frac{1}{3}\frac{\dot{\rho}}{\rho}(\hat{C}_{12} + \hat{C}_{13} + \hat{C}_{33}) = -\dot{p} \tag{99}$$

In order to recover the same solution obtained using full stress, we must have:

$$\dot{p} = K_1\frac{\dot{\rho}}{\rho} \tag{100}$$

$$\dot{p} = K_2\frac{\dot{\rho}}{\rho} \tag{101}$$

where:

$$K_1 = \frac{1}{3}(\hat{C}_{11} + \hat{C}_{12} + \hat{C}_{13}) \tag{102}$$

$$K_2 = \frac{1}{3}(\hat{C}_{12} + \hat{C}_{13} + \hat{C}_{33}) \tag{103}$$

For the isotropic case:

$$K_1 = K_2 = K = \frac{E}{3(1-2\nu)} \tag{104}$$

but for the transversely isotropic case, these two bulk moduli differ since:

$$\hat{C}_{11} = AE_2(1-\nu_{23}\nu_{32}) \tag{105}$$

$$\hat{C}_{33} = AE_3(1-\nu_{12}^2) \tag{106}$$

$$A^{-1} = (1-\nu_{12}-2\nu_{23}\nu_{32})(1+\nu_{12}) \tag{107}$$

7 Anisotropic elasto-plastic response

7.1 Crook yield criterion

Crook draws on work by Hashagen and Borst [34] who elaborate on the Hoffman criterion [35] and introduced nine anisotropic strength coefficients: 3 for tension, 3 for compression, and 3 for shear. Crook normalized these nine parameters α_1 through α_9. Hoffman uses a frame with x-y in the isotropic bedding plane and the z-axis normal to the bedding plane. This maps directly to the Bower frame with "1-2" corresponding to "x-y" and "3" corresponding to "z". However, Hoffman does not use the Voigt order for stress, but instead $\boldsymbol{\sigma}^*$ with components ordered as [11 22 33 12 23 13] in the yield criterion given below, in which:

$$F(\boldsymbol{\sigma}, \epsilon_v^P) = \frac{1}{M^2}(F_1(\boldsymbol{\sigma}^*))^2 + \frac{1}{b^2}(F_2(p, \epsilon_v^P))^2 - a(\epsilon_v^P)^2 \tag{108}$$

where M is the critical state line slope, and $b = 1$ if $p \geq (p_t - a)$, and $b = \beta$ otherwise, β being a consolidation cap parameter. Crook found that the circular form of the isotropic Cam-Clay Burland yield in the π-plane did not agree with experimental data for weakly cemented rocks (See Figures 6 and 7). Therefore, he introduced a lode angle function $g(\theta)$ with a parameter ξ in the range $0.778 \leq \xi \leq 1.0$, to obtain better agreement with the data, thus defining F_1 as:

$$F_1(\boldsymbol{\sigma}^*) = \frac{g(\theta)}{2}\sqrt{\frac{1}{2}\boldsymbol{\sigma}^{*\boldsymbol{T}}\boldsymbol{P}_{\boldsymbol{orth}}\boldsymbol{\sigma}^*} \tag{109}$$

$$\theta = \frac{1}{3}Sin^{-1}(\frac{3\sqrt{3}}{2}\frac{J_3'}{(J_2')^{3/2}}) \tag{110}$$

$$g(\theta) = [(1 + 1/\xi) - (1 - 1/\xi)sin(3\theta)] \tag{111}$$

Of the nine normalized strength parameters, the first three are used in F_2 according to the centering of the yield surface:

$$F_2(p, \epsilon_v^P) = \alpha_1\sigma_{11} + \alpha_2\sigma_{22} + \alpha_3\sigma_{33} - p_t(\epsilon_v^P) + a(\epsilon_v^P) \tag{112}$$

Since the yield surface is centered on the hydrostatic axis:

$$\alpha_1 = \alpha_2 = \alpha_3 = \frac{1}{3} \tag{113}$$

$$F_2(p, \epsilon_v^P) = p - p_t(\epsilon_v^P) + a(\epsilon_v^P) \tag{114}$$

In the initial version of the code, the yield formulation has been simplified so that:

$$\beta = 0 \tag{115}$$

$$p_t = 0 \tag{116}$$

$$b = 1 \tag{117}$$

Then a and F_2 have the form:

$$a = -p_c(\epsilon_v^P) \tag{118}$$

$$F_2(p, \epsilon_v^P) = p - p_c(\epsilon_v^P) \tag{119}$$

The yield in Eq. 108 thus takes the form:

$$F(\boldsymbol{\sigma}, p_c) = F_1^2(\boldsymbol{\sigma}) + (p - p_c)^2 - (p_c)^2 \tag{120}$$

$$F_1^2(\boldsymbol{\sigma}) = (\frac{g(\boldsymbol{S})}{2M})^2 T(\boldsymbol{\sigma}) \tag{121}$$

where $T(\boldsymbol{\sigma})$ is given by

$$T(\boldsymbol{\sigma}) = \frac{1}{2}\boldsymbol{\sigma^T P_V \sigma} \tag{122}$$

and $g(\boldsymbol{S})$ is given by:

$$g(\boldsymbol{S}) = [(1 + 1/\xi) - (1 - 1/\xi)(\frac{3\sqrt{3}}{2}\frac{J_3'(\boldsymbol{S})}{(J_2'(\boldsymbol{S}))^{3/2}})] \tag{123}$$

where $\boldsymbol{P_V}$ is derived from $\boldsymbol{P_{orth}}$ in Eq. 109 by rearranging only the components of $\boldsymbol{\Gamma_{orth}}$ to follow Voigt order.
For the general orthotropic case, we have:

$$\boldsymbol{P_V} = \begin{pmatrix} \boldsymbol{\Omega_V} & \boldsymbol{O} \\ \boldsymbol{O} & \boldsymbol{\Gamma_V} \end{pmatrix} \tag{124}$$

$$\boldsymbol{\Omega_V} = \begin{pmatrix} 2(\alpha_4+\alpha_6) & -2\alpha_4 & -2\alpha_6 \\ -2\alpha_4 & 2(\alpha_4+\alpha_5) & -2\alpha_5 \\ -2\alpha_6 & -2\alpha_5 & 2(\alpha_5+\alpha_6) \end{pmatrix} = \begin{pmatrix} 4\alpha_4 & -2\alpha_4 & -2\alpha_4 \\ -2\alpha_4 & 2(\alpha_4+\alpha_5) & -2\alpha_5 \\ -2\alpha_4 & -2\alpha_5 & 2(\alpha_4+\alpha_5) \end{pmatrix} \tag{125}$$

$$\boldsymbol{\Gamma_V} = \begin{pmatrix} 6\alpha_8 & 0 & 0 \\ 0 & 6\alpha_7 & 0 \\ 0 & 0 & 6\alpha_9 \end{pmatrix} = \begin{pmatrix} 4(2\alpha_4+\alpha_5) & 0 & 0 \\ 0 & 6\alpha_7 & 0 \\ 0 & 0 & 6\alpha_7 \end{pmatrix} \tag{126}$$

For the transversely isotropic case:

$$\alpha_6 = \alpha_4 \tag{127}$$

$$\alpha_9 = \alpha_7 \tag{128}$$

$$\alpha_8 = \frac{2}{3}(2\alpha_4 + \alpha_5) \tag{129}$$

and for the isotropic case:

$$\alpha_4 = \alpha_5 = \alpha_6 = \frac{1}{2} \tag{130}$$

$$\alpha_7 = \alpha_8 = \alpha_9 = 1 \tag{131}$$

in which case:

$$\frac{1}{2}\boldsymbol{\sigma^T P_V \sigma} = 3J_2' = q^2 \tag{132}$$

Crook's choices for alpha coefficients for Pierre 1 shale are given by:

$$\alpha_4 = 0.47 \tag{133}$$
$$\alpha_5 = 0.53 \tag{134}$$
$$\alpha_7 = 1.02 \tag{135}$$

7.2 Statement of problem for transversely isotropic elasto-plastic material

$$F(\boldsymbol{\sigma}, p_c) = (\frac{g(\boldsymbol{S})}{2M})^2 T(\boldsymbol{\sigma}) + (p - p_c)^2 - (p_c)^2 \tag{136}$$
$$g(\boldsymbol{S}) = [(1 + 1/\xi) - (1 - 1/\xi)(\frac{3\sqrt{3}}{2}\frac{J_3'(\boldsymbol{S})}{(J_2'(\boldsymbol{S}))^{3/2}})] \tag{137}$$
$$T(\boldsymbol{\sigma}) = \frac{1}{2}\boldsymbol{\sigma}^{\boldsymbol{T}}\boldsymbol{P_V}\boldsymbol{\sigma} \tag{138}$$
$$\tag{139}$$

Given strain rate $\dot{\epsilon}$, time step Δt, with old state $(\boldsymbol{\sigma}^n, \boldsymbol{\epsilon}^{P(n)}, p_c^n)$ satisfying:

$$F(\boldsymbol{\sigma}^n, p_c^n) \leq 0 \tag{140}$$

where $p_c(\epsilon_v^P)$ is defined in Section 8.3, and with trial stress state:

$$\tilde{\boldsymbol{\sigma}} = \boldsymbol{\sigma}^n + \boldsymbol{C} : \dot{\boldsymbol{\epsilon}}\Delta t \tag{141}$$

such that:

$$F(\tilde{\boldsymbol{\sigma}}, p_c^n) > 0 \tag{142}$$

Find new state: $(\boldsymbol{\sigma}^{n+1}, \boldsymbol{\epsilon}^{P(n+1)}, p_c^{n+1})$ such that:

$$F(\boldsymbol{\sigma}^{n+1}, p_c^{n+1}) = 0 \tag{143}$$

with

$$\boldsymbol{\sigma}^{n+1} = \boldsymbol{\sigma}^n + \dot{\boldsymbol{\sigma}}\Delta t \tag{144}$$
$$\dot{\boldsymbol{\sigma}} = \boldsymbol{C} : (\dot{\boldsymbol{\epsilon}} - \dot{\boldsymbol{\epsilon}}^P) \tag{145}$$
$$\boldsymbol{\epsilon}^{P(n+1)} = \boldsymbol{\epsilon}^{P(n)} + \dot{\boldsymbol{\epsilon}}^P\Delta t \tag{146}$$
$$\dot{\boldsymbol{\epsilon}}^P = \dot{\lambda}\frac{\partial F}{\partial \boldsymbol{\sigma}} \tag{147}$$
$$\tag{148}$$

where $\dot{\lambda}$ satisfies consistency $dF = 0$ i.e.:

$$\frac{\partial F}{\partial \boldsymbol{\sigma}} : \dot{\boldsymbol{\sigma}} + \frac{\partial F}{\partial p_c}\dot{p_c} = 0 \tag{149}$$

from which:

$$\dot{\lambda} = \frac{\boldsymbol{N} : \boldsymbol{C} : \dot{\boldsymbol{\epsilon}}}{\boldsymbol{N} : \boldsymbol{C} : \boldsymbol{N} - \frac{\partial F}{\partial p_c}\frac{\partial p_c}{\partial \epsilon_v^P} tr(\boldsymbol{N})} \tag{150}$$

$$\boldsymbol{N} = \frac{\partial F}{\partial \boldsymbol{\sigma}} \tag{151}$$

7.3 Newton-Raphson scheme

The above system requires a Newton-Raphson solution scheme. Using the system of equations in Section 7.2 for the new state, we construct such a Newton-Raphson solution scheme to solve for $\Delta\lambda$ satisfying:

$$F(\Delta\lambda) = F(\boldsymbol{\sigma}^{n+1}, p_c^{n+1}) = 0 \tag{152}$$

The iteration scheme, with iteration index r is:

$$\Delta\lambda^{[r+1]} = \Delta\lambda^{[r]} - \frac{F(\Delta\lambda^{[r]})}{F'(\Delta\lambda^{[r]})} \tag{153}$$

$$F'(\Delta\lambda) = \frac{\partial F}{\partial \boldsymbol{\sigma}} : \frac{\partial \boldsymbol{\sigma}}{\partial \Delta\lambda} + \frac{\partial F}{\partial p_c}\frac{\partial p_c}{\partial \epsilon_v^P}\frac{\partial \epsilon_v^P}{\partial \Delta\lambda} \tag{154}$$

$$\frac{\partial \boldsymbol{\sigma}}{\partial \Delta\lambda} = -\boldsymbol{C} : \frac{\partial F}{\partial \boldsymbol{\sigma}} = -\boldsymbol{C} : \boldsymbol{N} \tag{155}$$

$$\frac{\partial F}{\partial p_c} = -2p \tag{156}$$

$$\frac{\partial \epsilon_v^P}{\partial \Delta\lambda} = tr(\boldsymbol{N}) \tag{157}$$

Therefore:

$$F'(\Delta\lambda) = -\boldsymbol{N} : \boldsymbol{C} : \boldsymbol{N} - 2p\frac{\partial p_c}{\partial \epsilon_v^P} tr(\boldsymbol{N}) \tag{158}$$

7.4 Calculation of gradients

The calculation of the gradient $\boldsymbol{N}$ will be defined with respect to the stress components arranged in Voigt order, with the single index k ranging from 1 to 6 corresponding to [11 22 33 23 13 12]. From Equ. 120

$$N^k = \frac{\partial F}{\partial \sigma^k} = \frac{2}{M^2} F_1 \frac{\partial F_1}{\partial \sigma^k} + 2(p - p_c)\frac{\partial p}{\partial \sigma^k} \tag{159}$$

where, for $k = 1, 2, 3$:

$$\frac{\partial p}{\partial \sigma^k} = \frac{1}{3} \tag{160}$$

and, for $k = 4, 5, 6$**:**

$$\frac{\partial p}{\partial \sigma^k} = 0 \tag{161}$$

Using Eq. 122, T **becomes:**

$$T = \frac{1}{2}(\sum_{i=1}^{3}\sum_{j=1}^{3}\sigma^i \Omega_V^{ij}\sigma^j + \sum_{i=4}^{6}\sum_{j=4}^{6}\sigma^i \Gamma_V^{(i-3)(j-3)}\sigma^j) \tag{162}$$

$$\frac{\partial F_1}{\partial \sigma^m} = \frac{1}{2}(\frac{\partial g}{\partial S^k}\frac{\partial S^k}{\partial \sigma^m}\sqrt{T} + g\frac{\partial \sqrt{T}}{\partial \sigma^m}) \tag{163}$$

$$\frac{\partial g}{\partial S^k} = -(1 - 1/\xi)(\frac{3\sqrt{3}}{2})((-3/2)J_3'(J_2')^{-1/2}\frac{\partial J_2'}{\partial S^k} + (J_2')^{-3/2}\frac{\partial J_3'}{\partial S^k}) \tag{164}$$

$$J_2' = (1/2)(S_1^2 + S_2^2 + S_3^2) + S_4^2 + S_5^2 + S_6^2 \tag{165}$$

$$J_3' = S_1 S_2 S_3 + 2S_4 S_5 S_6 - S_1 S_4^2 - S_2 S_5^2 - S_3 S_6^2 \tag{166}$$

For $k = 1, 2, 3$**:**

$$\frac{\partial J_2'}{\partial S^k} = S^k \tag{167}$$

For $k = 4, 5, 6$**:**

$$\frac{\partial J_2'}{\partial S^k} = 2S^k \tag{168}$$

For $k = 1, 2, 3$ **with** (k, l, m) **a cyclic permutation of** $1, 2, 3$**:**

$$\frac{\partial J_3'}{\partial S^k} = S^l S^m - (S^{k+3})^2 \tag{169}$$

$$\frac{\partial J_3'}{\partial S^{k+3}} = 2(S^{l+3}S^{m+3} - S^k S^{k+3}) \tag{170}$$

$$\frac{\partial \sqrt{T}}{\partial \sigma^m} = (1/4)\frac{R_m}{\sqrt{T}} \tag{171}$$

where, for $m = 1, 2, 3$**:**

$$R_m = 2\sum_{i=1}^{3}\Omega_V^{mi}\sigma^i \tag{172}$$

and for $m = 4, 5, 6$**:**

$$R_m = 2\sum_{j=4}^{6}\Gamma_V^{(m-3)(j-3)}\sigma^j \tag{173}$$

$$\frac{\partial S_{ij}}{\partial \sigma_{kl}} = (-1/3)\delta_{kl}\delta_{ij} + \delta_{ik}\delta_{jl} \tag{174}$$

from which:

$$B^{km} = \frac{\partial S^k}{\partial \sigma^m} \tag{175}$$

is given by:

$$\boldsymbol{B} = \begin{pmatrix} \boldsymbol{H} & O \\ O & \boldsymbol{I} \end{pmatrix} \tag{176}$$

where:

$$\boldsymbol{H} = \begin{pmatrix} (2/3) & (-1/3) & (-1/3) \\ (-1/3) & (2/3) & (-1/3) \\ (-1/3) & (-1/3) & (2/3) \end{pmatrix} \tag{177}$$

8 Wood-Borja elasto-plastic porosity model

This porosity model sets the stage for later introducing pore fluid pressure. This model assumes that the material consists of solid grains separated by voids. The solid grains behave elastically as they come into contact with each other. They may break, but this is outside the scope of this model. Thus, the material elastic response results directly from the elasticity of the grains. The material plastic response encompasses the evolving distribution of voids between the grains, as the grains slide past each other under given loading. The measure of plastic deformation is based only on this evolving void distribution.

8.1 Wood's measure of porosity

Given soil solid volume measure v_s and soil void (pore) volume measure v_p comprising total volume measure v, Wood [28] defines soil void ratio e, porosity n, and a volumetric measure written here as v_{Wood} thus:

$$e = \frac{v_p}{v_s} \tag{178}$$

$$n = \frac{e}{(1+e)} \tag{179}$$

$$v_{Wood} = 1 + e \tag{180}$$

By interpreting the void ratio at its differential limit, these volumetric measures can be related to Rubin's [36] corresponding measures. Namely, Rubin defines porosity ϕ as:

$$\phi = \frac{dv_p}{dv} \tag{181}$$

where

$$dv = dv_p + dv_s \tag{182}$$

so that:

$$e = \frac{dv_p}{dv_s} = \frac{\phi}{1-\phi} \tag{183}$$

$$n = \phi \tag{184}$$

$$v_{Wood} = 1 + e = \frac{1}{1-\phi} \tag{185}$$

However, Carroll [37] defined a measure of porosity α as:

$$\alpha = \frac{v}{v_s} = \frac{1}{1-\phi} \tag{186}$$

Note that in both Wood's soil model and Carroll's porous model, the solid material occupies a skeleton matrix. Therefore, interpreting Carroll's measure at the differential limit, Wood's volumetric measure reduces to:

$$v_{Wood} = \alpha \tag{187}$$

8.2 Wood's porous elastic response

Wood [29] defines the soil elastic changes in porosity during unloading and reloading as:

$$-\frac{d\alpha^E}{\alpha^E} = \frac{\kappa}{\alpha^E}\frac{dp_e}{p_e} \tag{188}$$

from which:

$$\alpha^E = \alpha_0^E - \kappa\ ln\Big(\frac{p_e(\alpha^E)}{p_e(\alpha_0^E)}\Big) \tag{189}$$

and where the effective pressure p_e is given by:

$$p_e = \frac{1}{3}\sigma_{kk} \tag{190}$$

and κ is a soil parameter characterizing the slope of the elastic unload/reload line. For example, for Bay Mud, Borja [38] gives a value of κ=0.054. Note that stress and strain are taken to be positive in compression.

It is possible to show from Wood's porous elastic relation that elastic changes in porosity are directly related to the solid grain elastic response. From Carroll [37], for dry (drained) material, with $\alpha = \alpha^E$:

$$p_e = \frac{p_s}{\alpha} \tag{191}$$

so that:

$$(1 - \frac{\kappa}{\alpha})\dot{\alpha} = -\kappa\frac{\dot{p_s}}{p_s} \tag{192}$$

Now $\alpha > 1$ and $\kappa \ll 1$ and Wood [29] defines a bulk modulus (interpreted here as the solid grain bulk modulus) as:

$$K_s = \frac{\alpha p_e}{\kappa} \tag{193}$$

so that:

$$\dot{\alpha} = -\frac{\dot{p_s}}{K_s} \tag{194}$$

With an EOS for isotropic grain of the form:

$$\dot{p_s} = K_s \frac{\dot{\rho_s}}{\rho_s} \tag{195}$$

we have:

$$\dot{\alpha} = -\frac{\dot{\rho_s}}{\rho_s} \tag{196}$$

8.3 Wood-Borja porous plastic response

Wood [29] defines porosity changes due to changes in volumetric plastic strain as:

$$-\frac{d\alpha^P}{\alpha^P} = d\epsilon_v^P \tag{197}$$

from which:

$$\alpha^P(\epsilon_v^P) = \alpha_0^P \exp\left(-(\frac{\epsilon_v^P - \epsilon_{v0}^P}{\Lambda - \kappa})\right) \tag{198}$$

The total porosity accumulates changes from both the elastic porosity α^E and the plastic porosity α^P.

Borja [38] defines the hardening law as:

$$\dot{p_c} = \frac{p_c}{\Lambda - \kappa}\dot{\epsilon}_v^P \tag{199}$$

From which:

$$p_c(\epsilon_v^P) = p_{c0} \exp(\frac{\epsilon_v^P - \epsilon_{v0}^P}{\Lambda - \kappa}) \tag{200}$$

The soil parameter Λ, introduced by Wood [28], is quoted the value 0.37 by Borja [38] for Bay Mud.

The volumetric plastic strain rate is determined from the flow rule:

$$\dot{\boldsymbol{\epsilon}}^{\boldsymbol{P}} = \dot{\lambda}\mathbf{N} \tag{201}$$

$$\mathbf{N} = \frac{\partial F}{\partial \boldsymbol{\sigma}} \tag{202}$$

$$\dot{\epsilon}_v^P = tr(\dot{\boldsymbol{\epsilon}}^{\boldsymbol{P}}) = \dot{\lambda} tr(\mathbf{N}) \tag{203}$$

9 Application of Newton-Raphson solution scheme to combined Crook-Wood-Borja model

9.1 Algorithm

In this section, we describe the application of the Newton-Raphson solution scheme (see Section 7.3) to the plastic response, using a "radial return" scheme to obtain an estimate of the first iterate. The

Wood-Borja model is applied to update the elastic and plastic parts of the porosity.

The iteration scheme, with iteration index r is:

$$\Delta\lambda^{(r+1)} = \Delta\lambda^{(r)} - \frac{F(\Delta\lambda^{(r)})}{F'(\Delta\lambda^{(r)})} \tag{204}$$

$$F'(\Delta\lambda^{(r)}) = -\boldsymbol{N} : \boldsymbol{C} : \boldsymbol{N} - 2\beta p_e p_c tr(\boldsymbol{N}) \tag{205}$$

$$\beta = \frac{1}{\Lambda - \kappa} \tag{206}$$

Before starting the iteration, we obtain an estimate for a starting value for the iteration by applying radial return to calculate gradients evaluated at the stress state reduced from the trial value to a value which satisfies the yield; i.e., we calculate a stress estimate $\boldsymbol{\sigma}^*$ satisfying the yield criterion:

$$\boldsymbol{\sigma}^* = \gamma\tilde{\boldsymbol{\sigma}} \tag{207}$$

$$\gamma : F(\gamma\tilde{\boldsymbol{\sigma}}, p_c^n) = 0 \tag{208}$$

Note that if the pressure is outside the yield criterion ellipse (i.e., if $p < 0$ or $p > 2p_c$) or if the stress magnitude is negligibly small, then we take the trial stress itself as a starting value. We then calculate the gradients $\boldsymbol{N}$ to the yield surface at this stress estimate $\boldsymbol{\sigma}^*$ or $\tilde{\boldsymbol{\sigma}}$ and $\Delta\lambda$ at the same stress state, from the consistency condition for the combined model as:

$$\Delta\lambda^{[0]} = \frac{\boldsymbol{N} : \boldsymbol{C} : \Delta\boldsymbol{\epsilon}}{\boldsymbol{N} : \boldsymbol{C} : \boldsymbol{N} + 2\beta p_e p_c tr(\boldsymbol{N})} \tag{209}$$

This starting value for the stress state is further refined by applying a procedure which will also be applied at each iteration, and at the end of the iteration, and calculates the following in three steps:

1. New estimate for the corrected elastic stress:

$$\boldsymbol{\sigma}^{[r+1]} = \tilde{\boldsymbol{\sigma}} - \Delta\lambda^{[r]}\boldsymbol{C} : \boldsymbol{N}^{[r]} \tag{210}$$

2. New estimates for increment in volumetric plastic strain and associated yield strength:

$$\Delta\epsilon_v^{P[r+1]} = \Delta\lambda^{[r]} tr(\boldsymbol{N}^{[r]}) \tag{211}$$

$$p_c^{[r+1]} = p_c^n \exp(\beta\Delta\epsilon_v^{P[r+1]}) \tag{212}$$

3. New estimates for yield and associated gradients, at the corrected elastic stress.

9.2 Triaxial compression elasto-plastic response for isotropic yield

Consider triaxial compression for transverse isotropic material so that laboratory vertical axis coincides with normal to bedding plane. Apply Crook simplified yield with $\xi = 1$, and isotropic α coefficients for $\mathbf{\Omega_V}$ and $\mathbf{\Gamma_V}$. We calculate the elasto-plastic response consisting of three phases (see Figure 12):
(a) Phase 1 (elastic): pure increase in pressure from zero to virgin strength
$p^* : 0 < p^* < 2p_{c0}$ **without deviatoric stress (Figure 13),**

$$\dot{\sigma}_1 = \dot{\sigma}_2 = \dot{\sigma}_3 \tag{213}$$

$$\Delta\epsilon_3 = \frac{p^*}{E_3}(1 - 2\nu_{32}) \tag{214}$$

$$\Delta\epsilon_1 = \Delta\epsilon_2 = \frac{p^*}{E_2}(1 - \nu_{12} - \nu_{23}) \tag{215}$$

followed by
(b) Phase 2 (elastic): pure increase in deviatoric stress (Figure 14), keeping pressure fixed at p^*.

$$\dot{\sigma}_1 = \dot{\sigma}_2 \tag{216}$$

$$\dot{\sigma}_3 = -2\dot{\sigma}_1 \tag{217}$$

$$\Delta\epsilon_3 = \frac{2}{3}\frac{Mq^*}{E_3}(1 + \nu_{32}) \tag{218}$$

$$\Delta\epsilon_1 = \Delta\epsilon_2 = -\frac{1}{3}\frac{Mq^*}{E_2}(2\nu_{23} - \nu_{12} + 1) \tag{219}$$

$$q^* = \sqrt{p^*(2p_{c0} - p^*)} \tag{220}$$

$$\nu_{23} = \nu_{32}\frac{E_2}{E_3} \tag{221}$$

(c) Phase 3 (plastic): extending Phase 2 into the plastic regime.
As we continue to apply the strain rates from Phase 2, the material yields (Figure 18), showing first softening (Figure 17), with negative volumetric plastic strain rate (Figure 16), but as pressure increases, volumetric plastic strain reaches a minimum and then increases as material now hardens, showing increasing strength (Figure 17). Note that $\Delta\lambda$ is always positive, as seen in Figure 15.

The evolution of Wood porosity is shown in two figures. Figure 21 shows the total porosity and the elastic porosity. The latter clearly dominates over the plastic portion, shown in Figure 22.

For convenience in specifying strain rates in the Geodyn driver, all Poisson's ratios were zeroed and p^* was taken to be $0.4p_{c0}$. With

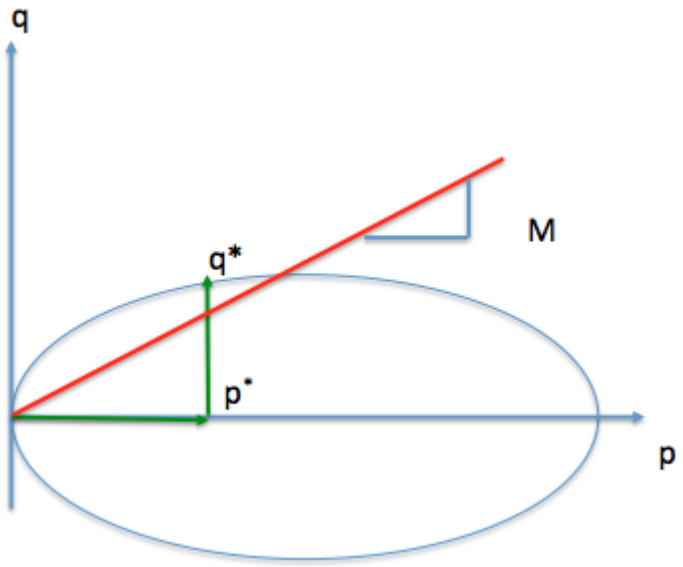

Figure 12: TXC stress path

$p_{c0} = 0.025$ **GPa,** $p^* = 0.01$ **GPa. The strain increments for reaching** p^* **are spread over 100 time steps of** 10^{-4} μsec**. With the Young's moduli** $E_2 = 2$ **GPa and** $E_3 = 1$ **GPa, the resulting strain rates were specified (per** μsec**) as:**

$$\dot{\epsilon}_1 = \dot{\epsilon}_2 = 0.5 \tag{222}$$

$$\dot{\epsilon}_3 = 1.0 \tag{223}$$

With these choices and setting the slope $M = 1$**, gives a convenient value for** $q^* = 0.02$ **GPa, the value of** q **when the stress first reaches the yield surface while the pressure is held fixed during Phase 2. From these values, we obtain convenient values for the strain rates during Phase 2 (spreading the strain increment 0.01 over 100 steps) as:**

$$\dot{\epsilon}_1 = \dot{\epsilon}_2 = -\frac{1}{3} \tag{224}$$

$$\dot{\epsilon}_3 = \frac{4}{3} \tag{225}$$

For these TXC calculations , given a maximum number of 50 iterations to reach 10^{-10} **error in yield relative to the trial yield, Figure 19 shows that the required tolerance (as shown in Figure 20) was reached in 7 iterations or less.**

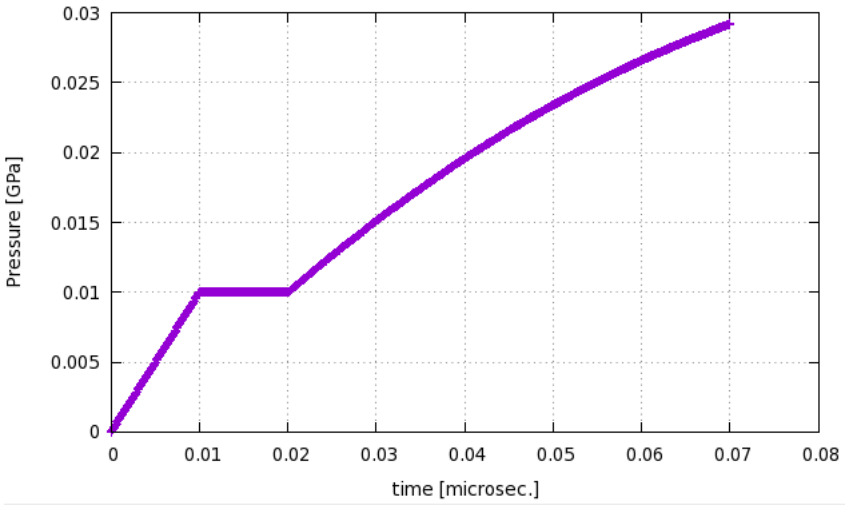

Figure 13: TXC pressure

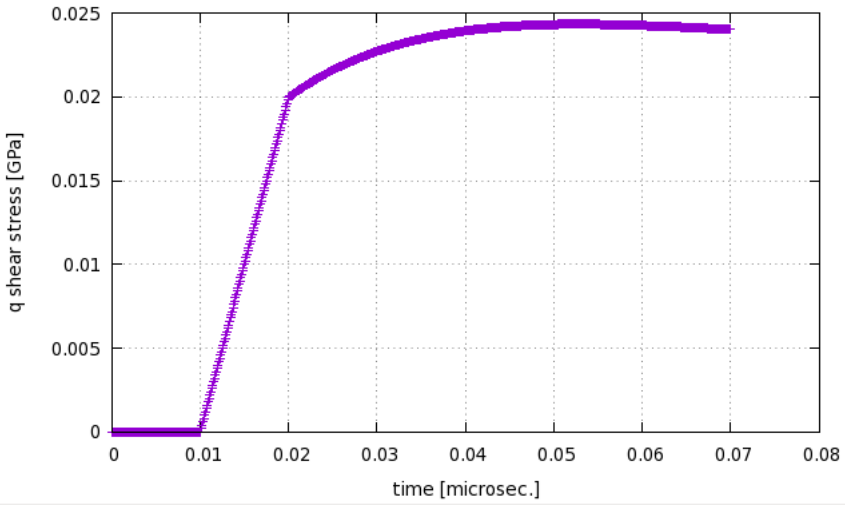

Figure 14: TXC q deviatoric stress

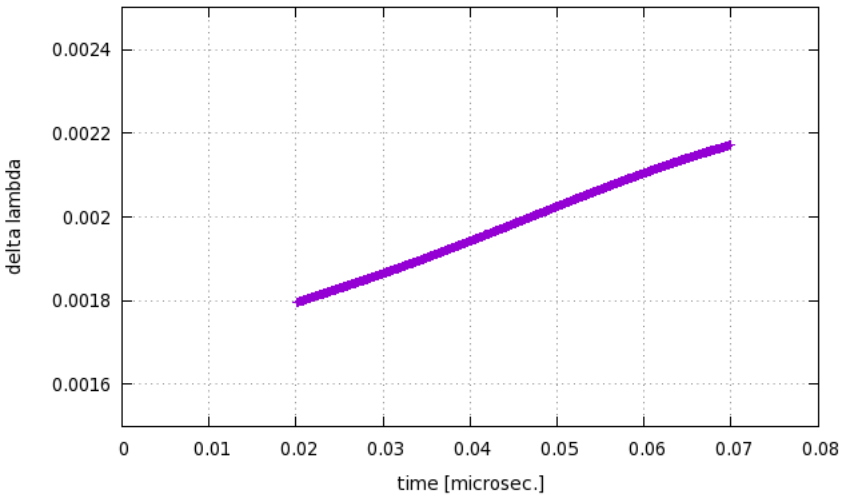

Figure 15: TXC delta lambda

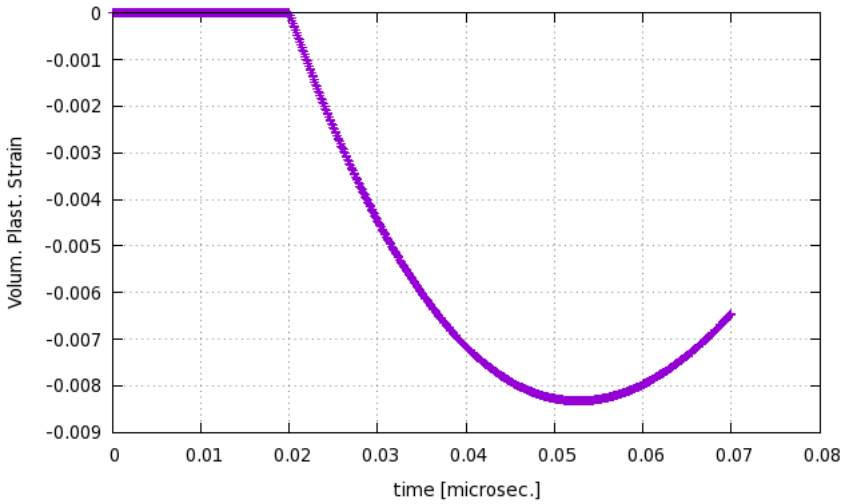

Figure 16: TXC volumetric plastic strain

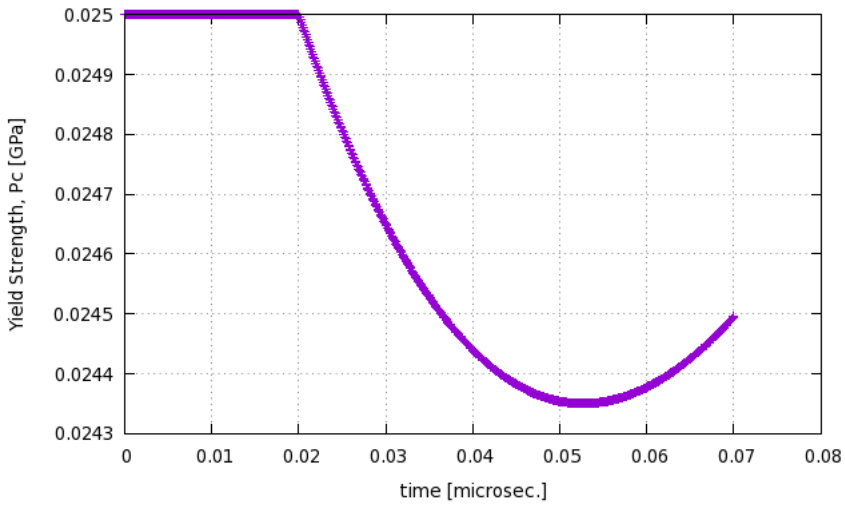

Figure 17: TXC yield strength Pc

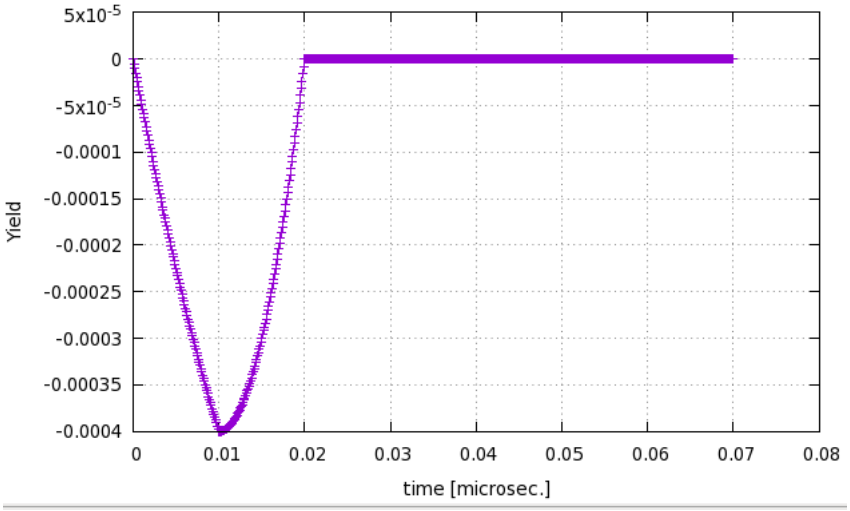

Figure 18: TXC yield criterion

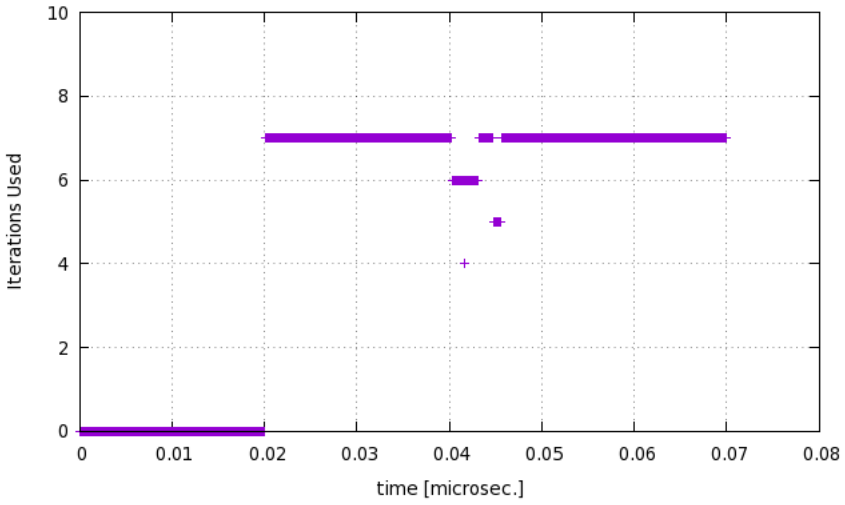

Figure 19: TXC Iterations Needed

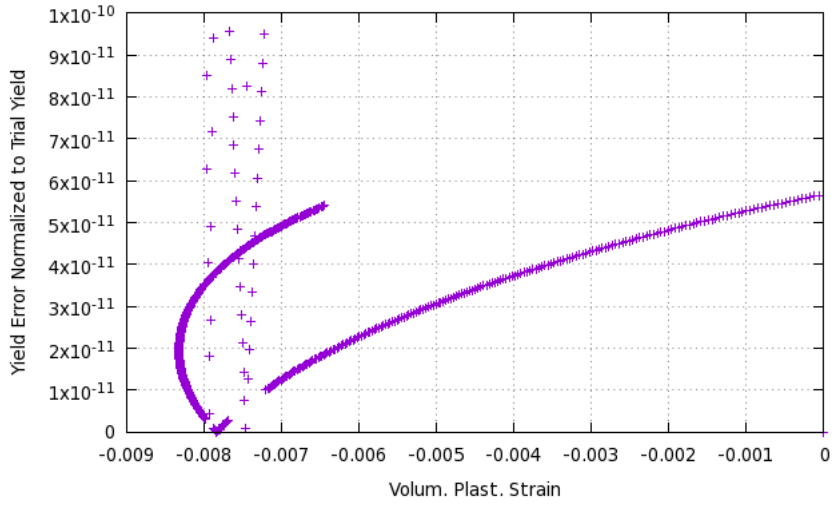

Figure 20: TXC yield error vs. vol. plast. strain

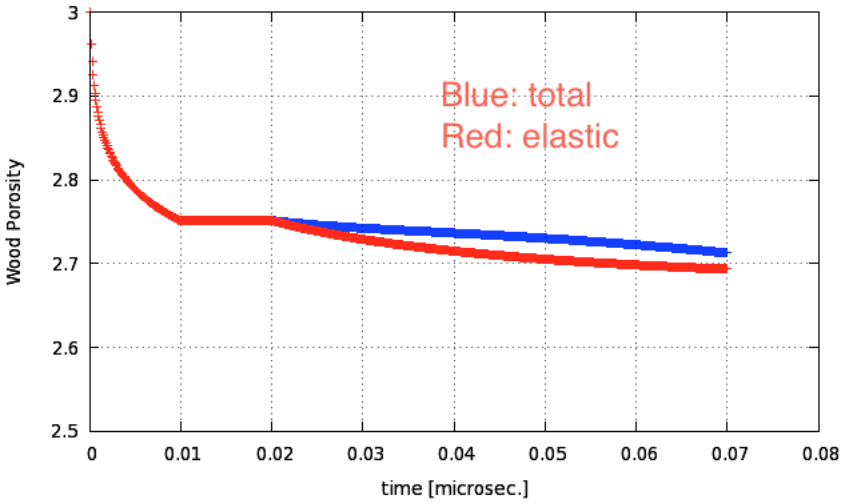

Figure 21: TXC total and elastic Wood porosity

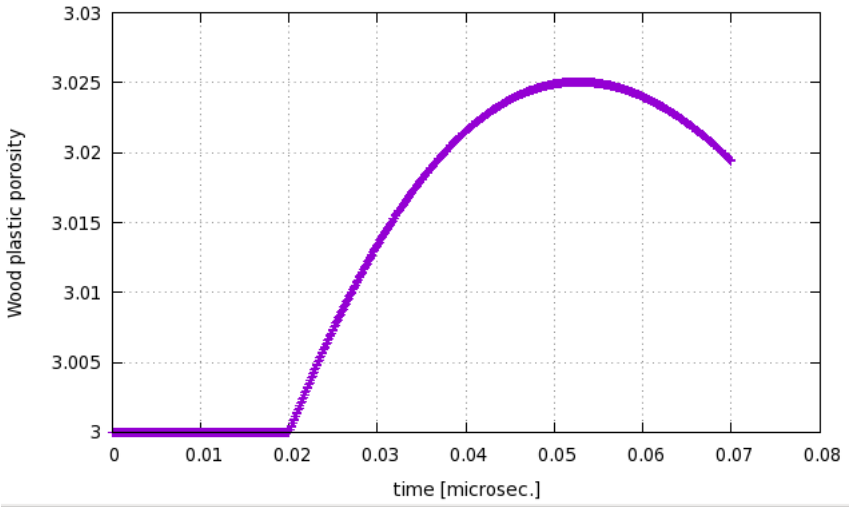

Figure 22: TXC Plastic Wood porosity

10 Implementation

The shale model has been implemented in C/C++ in the Geodyn driver.

10.1 Conventions

Notice that while stress is positive in compression in the shale model, the velocity gradient $\boldsymbol{L}$ is positive in tension, as specified in the Geodyn input deck. Therefore, given the Geodyn velocity gradient, we have to calculate the strain increment to be positive in compression as follows:

$$\boldsymbol{D} = -(1/2)(\boldsymbol{L} + \boldsymbol{L}^T) \tag{226}$$

$$\boldsymbol{W} = -(1/2)(\boldsymbol{L} - \boldsymbol{L}^T) \tag{227}$$

$$\Delta\boldsymbol{\epsilon} = \boldsymbol{D}\Delta t \tag{228}$$

Furthermore, all symmetric tensor quantities will be represented as a 6-component vector in Voigt order with the single index α ranging from 1 to 6 corresponding to [11 22 33 23 13 12].

10.2 Model input parameters

Note: Geodyn parameter names are shown in square brackets.

10.2.1 Elasticity parameters

Young's modulus normal to bedding plane, E_3 $[E3]$
Young's modulus within bedding plane, E_2 $[E2]$
Poisson's ratio out-of-plane, ν_{32} $[nu32]$
Poisson's ratio within bedding plane, ν_{12} $[nu12]$
Strike angle (usually 90 degrees) $[angle\_strike]$
Dip angle (degrees) of bedding plane $[angle\_dip]$
Initial Wood porosity ≥ 1 $[initial\_poro]$
Wood porous elastic slope κ $[soil\_kappa]$

10.2.2 Derived elasticity parameters

Poisson's ratio ν_{23} derived using Eq. 14.
Out-of-plane shear modulus G_3 derived using Eq. 18.

10.2.3 Plasticity parameters

Cam-clay parameter (dimensionless), ξ $[xi]$
Critical state line slope (dimensionless), M $[M]$

Orthotropic parameters (dimensionless), α_4**,** α_5**,** α_7 $[alpha4, alpha5, alpha7]$
Consolidation pressure p_{c0} **(pressure units)** $[pc0]$
Wood porous plastic slope, Λ **, dimensionless** $[soil\_lambda]$
Maximum number of iterations allowed in Newton-Raphson iteration $[maxiter]$
Newton-Raphson tolerance on normalized yield required $[NRtoler]$

10.3 Model history variables

Note: Geodyn variable names are shown in square brackets.
Yield strength, P_c $[Pc]$
Plastic strain ϵ_v^P $[plastic\_strain]$
Pressure p $[p]$
Yield Y $[Y]$
Flow parameter λ $[plastic\_lambda]$
Stress σ_{11} **etc...** $[TT11]$ **etc ... positive in compression.**
Strain ϵ_{11} **etc...** $[EvT11]$ **etc ... positive in compression**
Anisotropic longitudinal sound speed $[aniso\_sound\_speed]$
Radial return fraction γ $[scaling\_ratio]$
Shear stress q $[q]$
Wood total porosity α $[poroWood]$
Wood elastic porosity α^E $[poroElas]$
Wood plastic porosity α^P $[poroPlas]$
Number of iterations used r $[iterused]$
Yield error relative to trial yield $[yieldError]$

10.4 Model interaction with user EOS

Currently, the shale model as implemented does not apply a user-specified EOS, such as Gruneisen EOS, because of the issues described in Section 6.3.7. The pressure is determined only from the constitutive model for the full stress, allowing for elastic behavior subject to the yield criterion which constrains both the stress deviators and the pressure p**. This model must not be used for energetic materials.**

This work was performed under the auspices of the U.S. Department of Energy by Lawrence Livermore National Laboratory under Contract DE-AC52-07NA27344.

References

[1] **Aadnoy B. Modeling of the stability of highly inclined boreholes in anisotropic rock formations (includes associated papers 19213 and 19886). *SPE drilling engineering* 1988; 3(3):259–268.**

[2] **Cazacu O, Shao J, Henry J, Cristescu N. Elastic/viscoplastic constitutive equation for anisotropic shale. *2nd North American Rock Mechanics Symposium*, 1996.**

[3] **Søreide O, Bostrøm B, Horsrud P. Borehole stability simulations of an hpht field using anisotropic shale modeling. *Proceedings of the ARMA conference, Asheville, North Carolina*, 2008.**

[4] **Aoki T, Tan C, T COX R, Bamford W. Determination of anisotropic poroelastic parameters of a transversely isotropic shale by means of consolidated undrained triaxial tests. *8th ISRM Congress*, 1995.**

[5] **Crook A, Jian-Guo Y, Willson S. Development of an orthotropic 3d elastoplastic material model for shale. *SPE/ISRM Rock Mechanics Conference*, 2002.**

[6] **Islam M, Skalle P, Al-Ajmi A, Søreide O. Stability analysis in shale through deviated boreholes using the mohr and mogi-coulomb failure criteria. *44th US Rock Mechanics Symposium and 5th US Canada Rock Mechanics Symposium*, 2010.**

[7] **Grady D, Kipp M. Continuum modelling of explosive fracture in oil shale. *International Journal of Rock Mechanics and Mining Sciences & Geomechanics Abstracts*, vol. 17, Elsevier, 1980; 147–157.**

[8] **Kipp M, Grady D. Numerical studies of rock fragmentation. *Technical Report*, Sandia Labs., Albuquerque, NM (USA) 1980.**

[9] **Kipp M, Grady D, Chen E. Strain-rate dependent fracture initiation. *International Journal of Fracture* 1980; 16(5):471–478.**

[10] **Taylor LM, Chen EP, Kuszmaul JS. Microcrack-induced damage accumulation in brittle rock under dynamic loading. *Computer Methods in Applied Mechanics and Engineering* 1986; 55(3):301–320.**

[11] **Zhang YQ, Hao H, Lu Y. Anisotropic dynamic damage and fragmentation of rock materials under explosive loading. *International Journal of Engineering Science* 2003; 41(9):917–929.**

[12] **Nova R. An extended cam clay model for soft anisotropic rocks. *Computers and Geotechnics* 1986; 2(2):69–88.**

[13] **Niandou H, Shao J, Henry J. Anisotropic yield and failure of shale. *Assessment and Prevention of Failure Phenomena in Rock Engineering: Proceedings of the International Symposium on Assessment and Prevention of Failure Phenomena in Rock Engineering: Istanbul, Turkey, 5-7 April 1993*, Taylor & Francis, 1993; 107.**

[14] **Niandou H, Shao J, Henry J, Fourmaintraux D. Laboratory investigation of the mechanical behaviour of tournemire shale. *International Journal of Rock Mechanics and Mining Sciences* 1997; 34(1):3–16.**

[15] **Cazacu O, Cristescu N. A paraboloid failure surface for transversely isotropic materials. *Mechanics of materials* 1999; 31(6):381–393.**

[16] **Tien YM, Kuo MC. A failure criterion for transversely isotropic rocks. *International Journal of Rock Mechanics and Mining Sciences* 2001; 38(3):399–412.**

[17] **Pietruszczak S, Lydzba D, Shao JF. Modelling of inherent anisotropy in sedimentary rocks. *International journal of solids and structures* 2002; 39(3):637–648.**

[18] **Gao Z, Zhao J, Yao Y. A generalized anisotropic failure criterion for geomaterials. *International Journal of Solids and Structures* 2010; 47(22):3166–3185.**

[19] **Chen L, Shao JF, Huang H. Coupled elastoplastic damage modeling of anisotropic rocks. *Computers and Geotechnics* 2010; 37(1):187–194.**

[20] **Chen L, Shao J, Zhu Q, Duveau G. Induced anisotropic damage and plasticity in initially anisotropic sedimentary rocks. *International Journal of Rock Mechanics and Mining Sciences* 2012; 51:13–23.**

[21] **Hu D, Zhou H, Zhang F, Shao J, JF Z, *et al.*. Modeling of inherent anisotropic behavior of partially saturated clayey rocks. *Computers and Geotechnics* 2013; 48:29–40.**

[22] **Lisjak A, Tatone BS, Grasselli G, Vietor T. Numerical modelling of the anisotropic mechanical behaviour of opalinus clay at the laboratory-scale using fem/dem. *Rock Mechanics and Rock Engineering* 2012; :1–20.**

[23] **Dewhurst DN, Sarout JN, Piane CD, Siggins AF, Raven MD, Kuila UN. Prediction of shale mechanical properties from global and local empirical correlations. *2010 SEG Annual Meeting*, 2010.**

[24] **Sone H, Zoback M. Strength, creep and frictional properties of gas shale reservoir rocks. *44th US Rock Mechanics Symposium and 5th US-Canada Rock Mechanics Symposium*, 2010.**

[25] **Li Q, Chen M, Jin Y, Zhou Y, Wang F, Zhang R. Rock mechanical properties of shale gas reservoir and their influences on hydraulic fracture. *IPTC 2013: International Petroleum Technology Conference*, 2013.**

[26] **Carroll M. An effective stress law for anisotropic elastic deformation. *Journal of Geophysical Research: Solid Earth (1978–2012)* 1979; 84(B13):7510–7512.**

[27] **Chen Q, Nur A. Pore fluid pressure effects in anisotropic rocks: mechanisms of induced seismicity and weak faults. *pure and applied geophysics* 1992; 139(3-4):463–479.**

[28] **Wood D. *Soil behaviour and critical state soil mechanics*. Cambridge University Press, 1990.**

[29] **Wood D. *Geotechnical modelling*. Spon press, 2004.**

[30] **Bower AF. *Applied mechanics of solids*. CRC press, 2011.**

[31] **Ting T. *Anisotropic elasticity: theory and applications*. Oxford University Press, 1996.**

[32] **Saint Venant B. Sur la distribution des élasticités autour de chaque point d'un solide ou d'un milieu de contexture quelconque, particulièrement lorsqu'il est amorphe sans être isotrope. *Journal de Math. Pures et Appliquées* 1863; :257–430.**

[33] **Thomsen L. Weak elastic anisotropy. *Geophysics* October 1986; 51(10):1954–1966.**

[34] **Hashagen F, De Borst R. Enhancement of the hoffman yield criterion with an anisotropic hardening model. *Computers & Structures* 2001; 79(6):637–651.**

[35] **Hoffman O. The brittle strength of orthotropic materials. *Journal of Composite Materials* 1967; 1(2):200–206.**

[36] **Rubin M. Modeling added compressibility of porosity and the thermomechanical response of wet porous rock with application to mt. helen tuff. *International Journal of Solids and Structures* 1996; 33(6):761–793.**

[37] **Carroll M. Suggested modification of the p-alpha model for porous materials. *Journal of Applied Physics* February 1972; 43(2):759–761.**

[38] Borja RI, Lee SR. Cam-clay plasticity, part 1: implicit integration of elasto-plastic constitutive relations. ***Computer Methods in Applied Mechanics and Engineering*** **1990; 78(1):49–72.**